

## MATERIALS SCIENCE

# A highly efficient atomically thin curved PdIr bimetallic electrocatalyst

Fan Lv<sup>1,†</sup>, Bolong Huang<sup>3,†</sup>, Jianrui Feng<sup>1</sup>, Weiyu Zhang<sup>1</sup>, Kai Wang<sup>1</sup>, Na Li<sup>4,5</sup>,  
Jinhui Zhou<sup>1</sup>, Peng Zhou<sup>1</sup>, Wenxiu Yang<sup>1</sup>, Yaping Du<sup>6</sup>, Dong Su<sup>5</sup>  
and Shaojun Guo<sup>1,2,\*</sup>

<sup>1</sup>School of Materials Science and Engineering, Peking University, Beijing 100871, China;

<sup>2</sup>College of Engineering, Peking University, Beijing 100871, China;

<sup>3</sup>Department of Applied Biology and Chemical Technology, Hong Kong Polytechnic University, Hong Kong, China;

<sup>4</sup>Frontier Institute of Science and Technology jointly with College of Science, Xi'an Jiaotong University, Xi'an 710054, China;

<sup>5</sup>Center for Functional Nanomaterials Brookhaven National Laboratory, Upton, NY 11973, USA and

<sup>6</sup>School of Materials Science and Engineering & National Institute for Advanced Materials, Nankai University, Tianjin 300350, China

**\*Corresponding author.**

E-mail: [guosj@pku.edu.cn](mailto:guosj@pku.edu.cn)

<sup>†</sup>Equally contributed to this work.

Received 5 January 2021; Accepted 23 January 2021

**ABSTRACT**

The multi-metallene with an ultrahigh surface area has great potential in precise tuning of surface heterogeneous d-electronic correlation by surface strain effect for the distinctive surface electronic structure, which is a brand new class of promising 2D electrocatalyst for sustainable energy device application. However, achieving such an atomically thin multi-metallene still presents a great challenge. Herein, we present a new synthetic method for an atomic-level palladium-iridium (PdIr) bimetallic with an average thickness of only  $\sim 1.0$  nm for achieving superior catalysis in the hydrogen evolution reaction (HER) and the formic acid oxidation reaction (FAOR). The curved PdIr bimetallic presents a top-ranked high electrochemical active area of  $127.5 \pm 10.8 \text{ m}^2 \text{ g}_{\text{Pd+Ir}}^{-1}$  in the reported noble alloy materials, and exhibits a very low overpotential, ultrahigh activity and improved stability for HER and FAOR. DFT calculation reveals that the PdIr bimetallic herein has a unique lattice tangential strain, which can induce surface distortion while concurrently creating a variety of concave-convex featured micro-active regions formed by variously coordinated Pd sites agglomeration. Such a strong strain effect correlates the abnormal on-site active  $4d^{10}$ - $t_{2g}$ -orbital Coulomb correlation potential and directly elevates orbital-electronegativity exposure within these active regions, resulting in a preeminent barrier-free energetic path for significant enhancement of FAOR and HER catalytic performance.

**Keywords:** strain, metallene, PdIr alloy, atomically thin, electrocatalyst

**INTRODUCTION**

Electrocatalysis will have a significant role in realizing the widespread use of renewable energy in future [1–3]. However, most catalysts used for renewable energy application still rely largely on the precious metals. To reduce the dependence on and massive depletion of these precious metals, great efforts have been devoted to searching for desirable electrocatalysts with the guidance of both/either increasing exposed active sites *per* mass and/or their intrinsic activity [4–6]. Regulation of the morphology [7–9] and composition [10–12] of catalysts are conventional methods to realize the above goals, with optimization of appropriate atomic number and electron distribution on the surface of these metallic catalysts being key to the achievement of more efficient catalytic performance.

Thin two-dimensional (2D) nanomaterials are a recently identified class of highly efficient catalysts [13–17]. Their merit for electrocatalysis is that most of their metal atoms are exposed on the surface to take part in the catalytic reaction, thus greatly improving the atomic utilization. Meanwhile, the exposure with specific facets on the surface, similar to the typical thin film system [18,19], makes it much easier to identify the active sites on the 2D nanomaterials for electrocatalysis, which can then be modeled by experiments or theoretical calculation. More importantly, thin 2D nanomaterials always exhibit a varied surface intrinsic electronic structure relative to their bulk or nanoparticle counterparts [20], and the overlapping degree of diverse electron orbitals on the surface could be more effectively regulated by atomic

surface-modification [21] and/or strain-engineering [22] because of the well-defined thin 2D structures. All these merits of thin 2D nanostructures equip them with good advantages to acquire the desirable surface atomic/electronic structure for electrocatalysis and establish the corresponding surface electronic structure-electrocatalytic property relationship. Very recently, it was observed that atomically thin 2D metals/alloys possess intrinsic strain related to their specific thickness [23] or curvature [24], which greatly modulates the surface electronic structure and energetics of reaction intermediates, which can then promote catalytic activities. However, because of great difficulties in synthesizing such suprather thin multi-metallic nanosheets (NSs) at few atomic thickness levels, such a concept is largely constrained in that it has not been well demonstrated or fully discussed.

Herein, we present a new strategy for synthesizing suprather thin, curved PdIr alloy NSs with around five atomic layers of thickness, in design of superior catalysts. Because of the structural analogy with graphene, in this study, we refer to the PdIr alloy NSs as 'PdIr bimetallic'. The PdIr bimetallic shows a very high electrochemically active surface area (ECSA,  $127.5 \pm 10.8 \text{ m}^2 \text{ g}_{\text{Pd+Ir}}^{-1}$ ) and unique surface electronic structure, enabling superior electrocatalytic performance for both the hydrogen evolution reaction (HER) with reduced overpotential of 34 mV at current density of  $10 \text{ mA cm}^{-2}$  relative to that of commercial Pt/C (78 mV), and the formic acid oxidation reaction (FAOR) with mass activity of  $2.7 \text{ A mg}_{\text{Pd+Ir}}^{-1}$  at 0.5 V vs reversible hydrogen electrode (RHE), 4.8 times higher than the commercial Pd/C. DFT calculations confirm that the surface strain effect endows the PdIr bimetallic with exceptional modulation ability of surface electronic structures within the concave-convex featured micro-active regions for higher electroactivity. Thus, excellent HER and FAOR performances originate from the optimized surface binding, in which the Pd-overbinding has been alleviated via Ir-5d  $t_{2g}$  suppression. Concurrently, the Ir-5d  $e_g$  activity ensures extraordinarily high OH-dissociation efficiency and stable  $\text{HCOO}^*$ -docking to achieve the prominent FAOR process. Therefore, the realization of bifunctional atomic d-band-tuning engineering has been excavated for optimal electrocatalytic performance of HER and FAOR.

## RESULTS AND DISCUSSION

Typical PdIr bimetallic was synthesized by reduction of palladium acetylacetonate ( $\text{Pd}(\text{acac})_2$ )

and continuous decomposition of tetrairidium dodecacarbonyl ( $\text{Ir}_4(\text{CO})_{12}$ ) in oleylamine (OAM) at  $150^\circ\text{C}$  (details in Methods). Representative low-magnification high-angle annular dark-field scanning transmission microscopy (HAADF-STEM) and transmission electron microscopy (TEM) images show that the obtained products are entirely composed of graphene-like NSs, which are either horizontal or vertical standing. As observed from vertical standing PdIr bimetallic, most have a lateral size of between 20 and 30 nm, with a specially curved structure (Fig. 1a and b). The ultrathin character of the PdIr bimetallic was further confirmed by high-magnification TEM and atomic force microscopy (AFM) measurements. Ultrathin nanostructures are usually very sensitive to electron beams under the common TEM testing environment [25,26]. In our case, pores appeared immediately on the horizontal standing NSs when they were subjected to high-magnification TEM, indicative of suprather thin thickness (Fig. S1). In addition, Fig. 1c shows a side view of several groups of NSs with lamellar structures. The thickness of the PdIr bimetallic is measured to be  $\sim 1 \text{ nm}$ , about five atomic layers thick, in agreement with high-resolution TEM (HRTEM) (Fig. S2) and AFM results (Fig. 1d). Aberration-corrected HAADF-STEM was performed to present the atomic-scale surface structure of one individual PdIr bimetallic (Fig. 1e). The corresponding fast Fourier transformation (FFT) pattern of the NS (inset of Fig. 1e) shows a 6-fold rotational symmetry structure of the PdIr bimetallic, denoting that the NS has a face-centered cubic (fcc) crystal structure stacked with (111) facets in the vertical direction [20]. Distinct lattice spacing of 0.23 nm from the enlarged image of one part of this NS can be assigned to the  $1/3$  (422) fringe of fcc structure (Fig. 1f). To analyze the elemental composition of the PdIr bimetallic, results from STEM energy dispersive X-ray spectroscopy (EDS) line scanning and mapping of single PdIr bimetallic are shown in Figs 1g and S3. The Pd and Ir elements are homogeneously distributed on the NS. The composition ratio of Pd to Ir in PdIr bimetallic is 77.3/22.7, as determined by inductively coupled plasma atomic emission spectroscopy (ICP-AES), consistent with the result of TEM-EDS (78.2/21.8). An X-ray photoelectron spectroscopy (XPS) result (Fig. 1h and i) further reveals that surface Pd and Ir in PdIr bimetallic are mainly in the metallic state, and the peaks of Pd 3d of PdIr bimetallic are clearly shifted to higher binding energy while the peaks of Ir 4f are shifted to lower binding energy, indicating electron transfer from Pd to Ir on the surface of PdIr bimetallic.

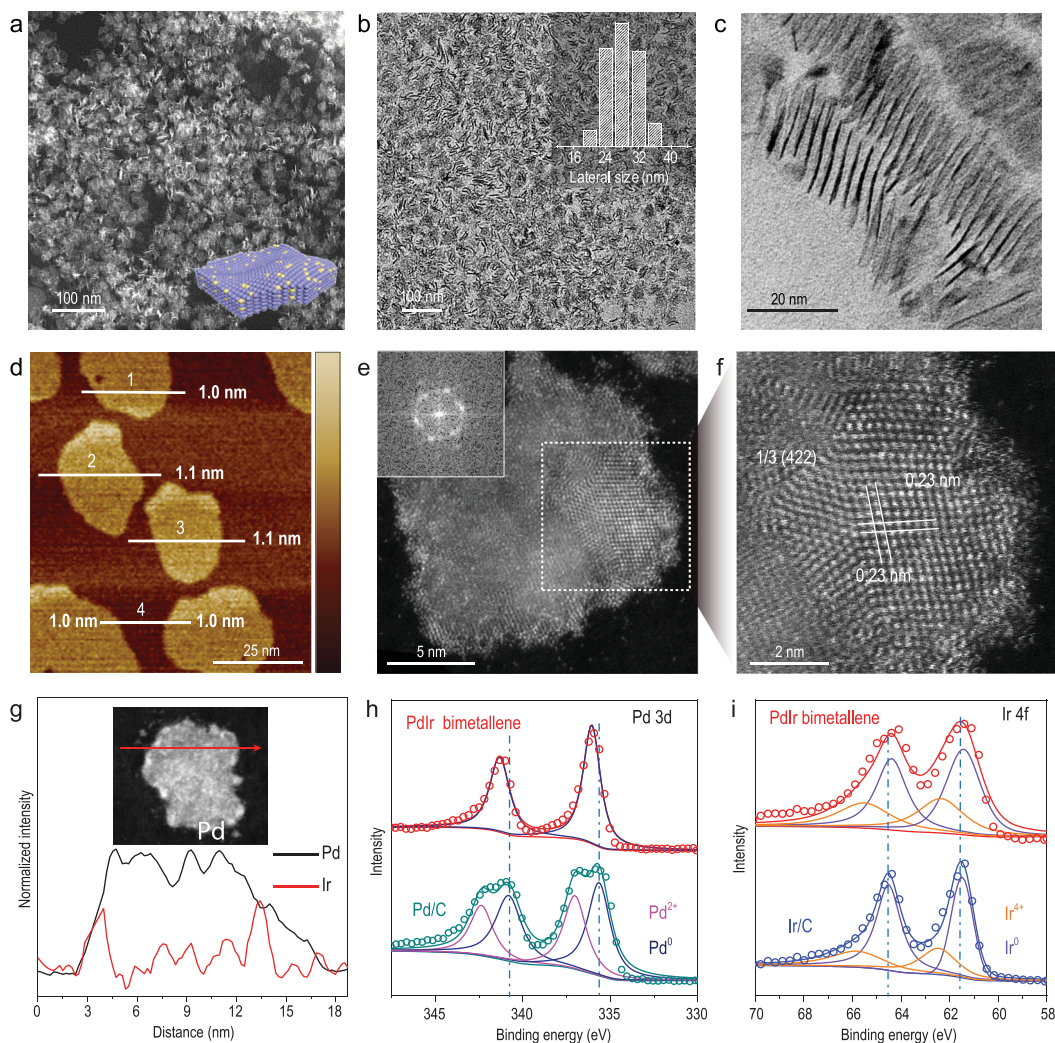


**Figure 1.** Morphology and phase characterization of PdIr bimetallic. (a) Low-magnification HAADF-STEM image. (b and c) TEM images and the lateral size distribution (inset of Fig. 1b) of PdIr bimetallic. (d) AFM and (e and f) HAADF-STEM images of PdIr bimetallic. (g) EDS linear scan of PdIr bimetallic for Pd and Ir elements. (h and i) XPS spectra of Pd 3d of PdIr bimetallic/C and commercial Pd/C, and Ir 4f of PdIr bimetallic/C and commercial Ir/C.

Time-dependent experiments were carried out to better understand the growth mechanism of PdIr bimetallic. TEM images of the products at different reaction time are displayed in Fig. 2a. The results show that a number of small NSs have already formed at the initial reaction stage (10 min). The lateral size of NSs continued to grow in the next hour, and then their morphology stayed almost unchanged. X-ray diffraction (XRD) and TEM-EDS were also performed to study the phase and elemental composition of these intermediates. The XRD patterns of these products all showed three typical *fcc* peaks and the peaks continuously shifted to higher angles as the reaction time proceeded from 1 to 8 h, indicating that more Ir atoms were alloyed with Pd metallene during the post-reaction stage (Fig. 2b). The alloying process could also be

traced from the atomic ratio of Pd and Ir, as calculated from TEM-EDS (Fig. 2c and d). At the first 10 min reaction, the obtained small NSs were basically composed of Pd. After that, the Ir(0) atoms, decomposed from  $\text{Ir}_4(\text{CO})_{12}$ , began to embed into the Pd metallene. The achieved highest atomic percentage of Ir element in PdIr bimetallic is almost 23% after 8 h, and did not further increase when extending reaction time to 12 h. When we changed the dosage of  $\text{Ir}_4(\text{CO})_{12}$  in the precursor, the atomic ratio of Pd/Ir in bimetallic could be tuned (Fig. S4). From ultraviolet-visible (UV-VIS) spectrums of the intermediate products, their absorption peaks show a negative shift over reaction time, attributed to change of surface electronic structure on the PdIr bimetallic during the alloying process (Fig. S5). Furthermore, we found that

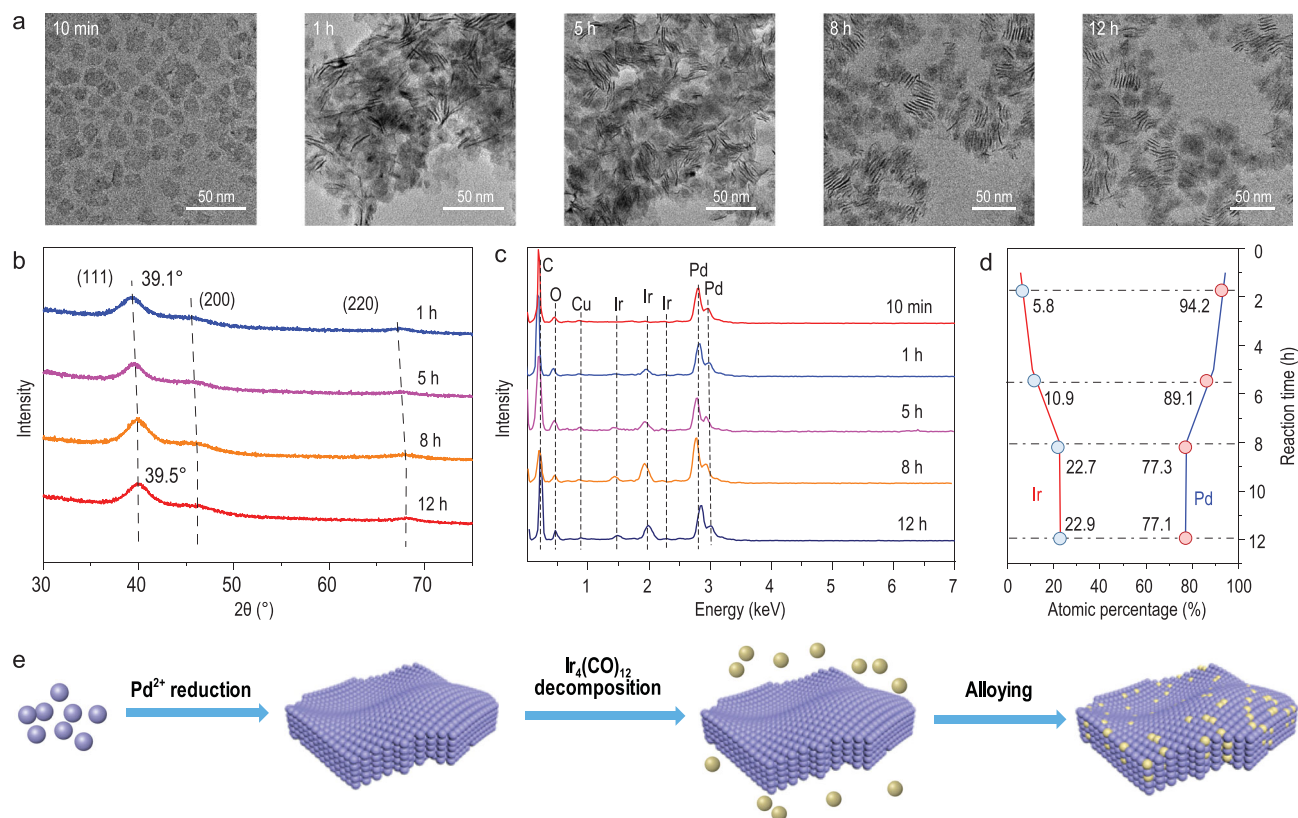


**Figure 2.** Time-dependent growth process of PdIr bimetallic nanosheet. (a) TEM images of products at different reaction time of 10 min, 1 h, 5 h, 8 h and 12 h, respectively. (b) XRD patterns of products at different reaction time. (c and d) EDS spectrums and the atomic ratio of Pd and Ir of the products at different reaction time. (e) Schematic illustration of the growth process of PdIr bimetallic nanosheet.

usage of  $\text{Ir}_4(\text{CO})_{12}$  was necessary for formation of PdIr bimetallic nanosheet. When substituting the  $\text{Ir}_4(\text{CO})_{12}$  with other iridium precursors and keeping other conditions consistent, a mixture of only irregular Pd NSs and tetrahedral Pd nanostructures was obtained (Fig. S6). Reduction of dissolved  $\text{Ir}^{3+}$  to  $\text{Ir}^0$  atoms in OAM solvent always required a high temperature ( $>200^\circ\text{C}$ ) [8,27], whereas Ir was detected in the products with the use of  $\text{Ir}_4(\text{CO})_{12}$  even when the temperature was lowered to  $100^\circ\text{C}$  (Fig. S7). In addition, the CO decomposed from the  $\text{W}(\text{CO})_6$  and  $\text{Ir}_4(\text{CO})_{12}$  in our method, served as a surface capping-agent, confining the growth of Pd (111) facets and resulting in the 2D structure [28–30]. Otherwise, PdIr nanoparticles (PdIr NP) were generated without adding  $\text{W}(\text{CO})_6$  (Fig. S8). We infer that the synthetic process of PdIr bimetallic nanosheet relied upon first reduction of  $\text{Pd}(\text{acac})_2$  to form Pd metallene, then decomposition of  $\text{Ir}_4(\text{CO})_{12}$  and finally diffusion of  $\text{Ir}^0$  atoms to the Pd NSs (Fig. 2e), similar to recently reported PdMo bimetallic nanosheet [24]. However, the Ir element is much more stable than the Mo element and can exist on the outer surface of PdIr bimetallic nanosheet, perhaps participating in the catalytic process as synergistic active

sites with Pd. Besides, based on the XRD measurements (Fig. S9), we noted that the peak indexed to the (111) plane of PdIr bimetallic nanosheet was located at  $39.5^\circ$ , smaller than those of the synthesized PdIr NP with identical atomic Pd/Ir ratio ( $40.2^\circ$ ), standard *fcc* Pd ( $40.11^\circ$ , JCPDS 46-1043) and Ir crystal ( $40.66^\circ$ , JCPDS 06-0598). Extended X-ray adsorption fine structure (EXAFS) analysis (Fig. S10 and Table S1) also revealed that the length of the Pd-Pd(Ir) bond in PdIr metallene is about 0.277 nm, larger than those in PdIr (0.274 nm) and Pd foil (0.274 nm). The strain of PdIr bimetallic nanosheet is therefore calculated to be 1.1%.

To further confirm the ultrathin structure of PdIr bimetallic nanosheet, the ECSA of the carbon supported PdIr bimetallic nanosheet (PdIr bimetallic nanosheet/C, Fig. S11) was firstly tested by cyclic voltammetry (CV) in 0.1 M  $\text{HClO}_4$  by integrating the charge of the  $\text{H}_{\text{upd}}$  desorption peak (Fig. S12). PdIr bimetallic nanosheet/C showed an ECSA of  $130.3 \pm 9.2 \text{ m}^2 \text{ g}_{\text{Pd+Ir}}^{-1}$ , much larger than those of carbon supported PdIr NP (PdIr NP/C,  $38.9 \pm 5.0 \text{ m}^2 \text{ g}_{\text{Pd+Ir}}^{-1}$ ), commercial Pd/C ( $38.6 \pm 2.8 \text{ m}^2 \text{ g}_{\text{Pd}}^{-1}$ ) and Pt/C ( $70.1 \pm 4.3 \text{ m}^2 \text{ g}_{\text{Pt}}^{-1}$ ). Pd can easily absorb hydrogen into its inner lattice, resulting in inaccuracies

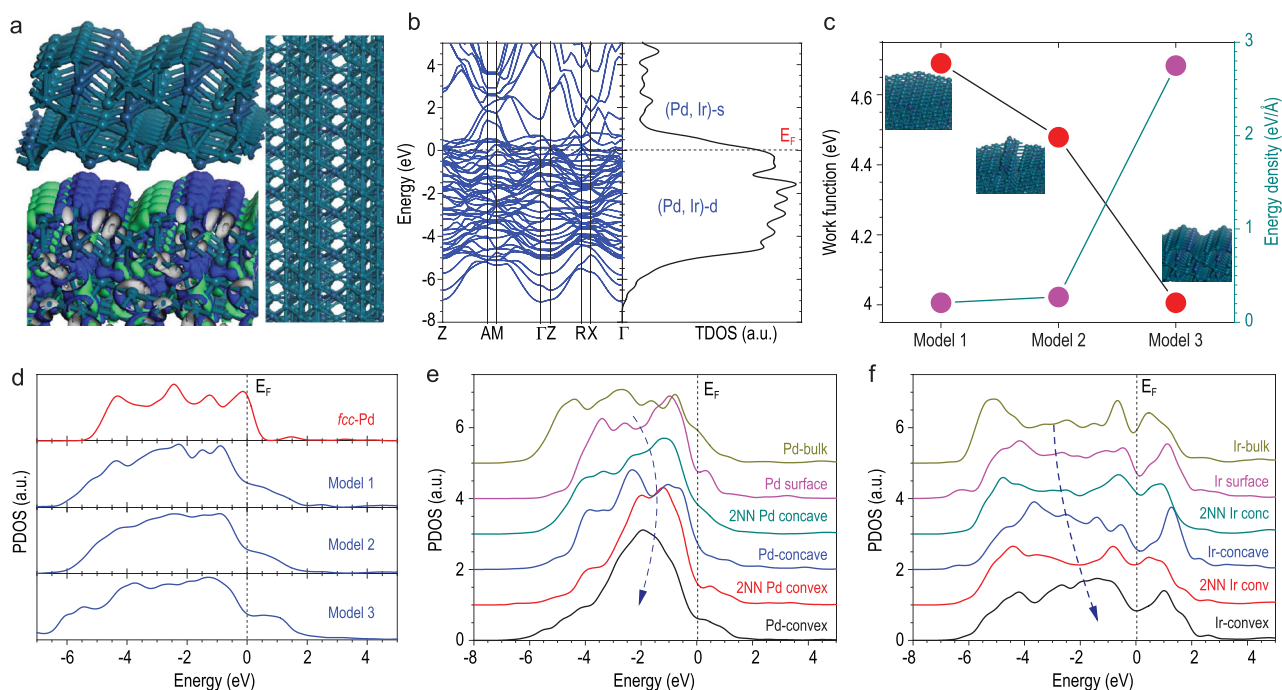


**Figure 3.** Theoretical calculation of the electron structure of the PdIr bimetallic. (a) The strained (111) surface lattice of the as-built  $\text{Pd}_8\text{Ir}_2$  structural model (model 3) with charge density distributions. (b) Band structure and total density of states (TDOSs) of the  $\text{Pd}_8\text{Ir}_2$  model. (c) Surface work functions and energy area density dependences are shown for three given surface models. (d) PDOSs of overall d-bands for *fcc*-Pd, model 1, 2 and 3 for illustrating strain modulation. (e) PDOSs of 4d bands of variously coordinated Pd sites exposing within concave-convex region. (f) PDOSs of 5d bands of variously coordinated Ir sites nearby those modulated Pd sites.

to the calculated ECSA. Thus, we applied CO stripping methods to calculate the ECSA of PdIr bimetallic/C, PdIr NP/C and commercial Pd/C (Fig. S13). The calculated ECSA results are summarized in Table S2, and the value of our synthesized PdIr bimetallic ( $127.5 \pm 10.8 \text{ m}^2 \text{ g}_{\text{Pd+Ir}}^{-1}$ ) still ranks the highest among recently reported Pd-based catalysts (Table S3).

Inspired by the atomically thin thickness and intrinsic strain resulting from the curve structure of PdIr bimetallic, we employed DFT calculations to project its underlying unique surface electronic structure. According to the above structure characterization of PdIr bimetallic, the surface (111) of  $\text{Pd}_8\text{Ir}_2$  structural model has been constructed with five-layer thickness. In creating the large dislocations and the generated strain applied parallel [111]-direction, there have been obvious (Pd-Ir)-reconstructed concave-convex featured distortions formed on the  $\text{Pd}_8\text{Ir}_2$  (111) surface with strip ripples (Fig. 3a). Local charge densities from electronic states near the Fermi level ( $E_F$ ) reflect that the concave-convex regions are the electro-active areas. The distortion character reflects a continuous and smooth variation trend in local features of the density of states (DOSs), showing clear tail states across the  $E_F$ . This confirms the absence of long-

range order in the lattice (Fig. 3b). With strain scale increased, the energy area density increases while the surface work function exhibits the inverse behavior, denoting enhanced electronic activity on the surface. This trend indicates that the surface on-site orbital Coulomb potential has been modulated as the electronic-activation barrier was lowered, showing a direct correlation with surface strain effect (Fig. 3c). Further analysis on the projected partial density of states (PDOSs) interprets that the overall d-band has been clearly modulated by the surface strain, shifting the lower position to alleviate the overbinding effect (Fig. 3d). We see that the surface strain effect evidently tunes the Pd-4d electronic characters from concave to convex to increase the selectivity. The 4d band center has downshifted from  $E_V$ -1.7 eV (concave) to  $E_V$ -2.6 eV (convex), referred to the strain-free PdIr surface ( $E_V$ -1.5 eV). Even the second nearest neighboring (2NN) Pd sites exhibited an obvious response to the strain-induced 4d variations (Fig. 3e). More contrast variation trend has been illustrated in Fig. S14. We further studied the role of Ir among different regions. The variation trend of the 5d-band implies an opposite trend to that of the related nearby Pd site. It indicates that the Ir-5d orbital not only disturbs the inter-d-orbital Coulomb potential distribution for

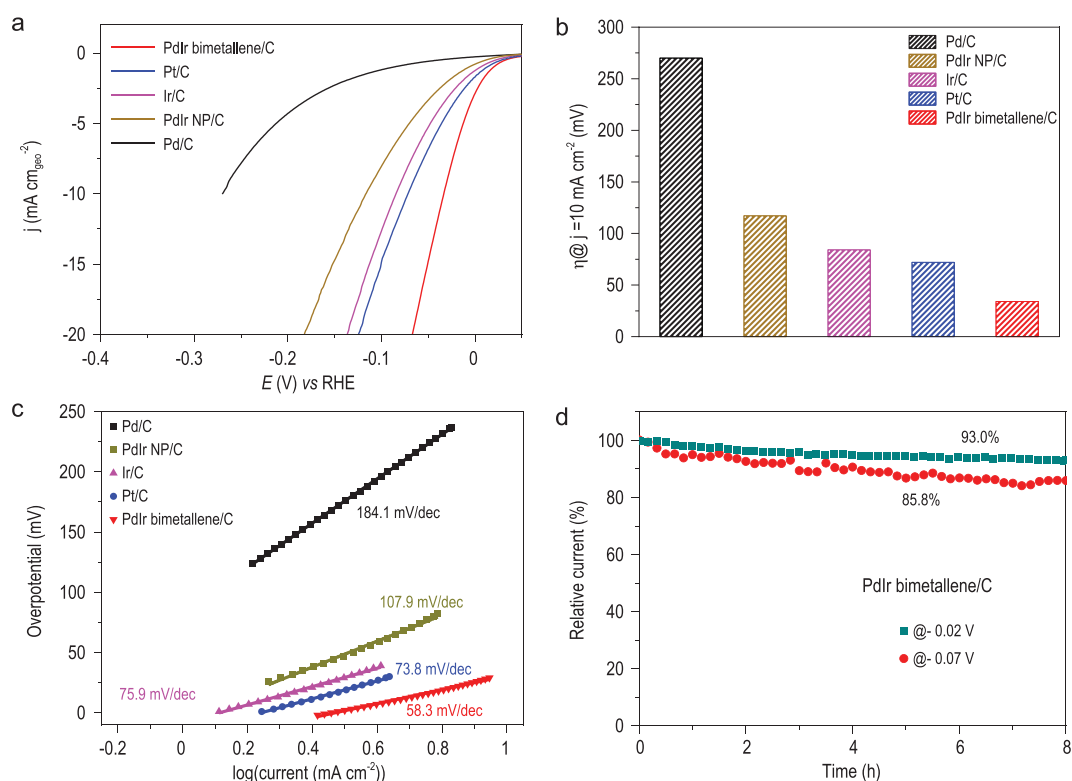


**Figure 4.** HER activity and durability of PdIr bimetallic in 0.1 M KOH. (a) HER polarization curves of PdIr bimetallic/C, PdIr NP/C, Ir/C, Pt/C and Pd/C at a scan rate of 5 mV s<sup>-1</sup> with 95% iR-compensation. (b and c) Overpotentials at 10 mA cm<sup>-2</sup> (b) and Tafel slopes (c) of different catalysts. (d) Chronoamperometric curves of the PdIr bimetallic/C catalysts at an applied potential of -0.02 and -0.07 V vs RHE.

generating the strain, but also acts as an electron relay center to associate site-to-site electron transfer of Pd site (Fig. 3f), which is a deep interpretation from the XPS results. And the surface strain causes the Ir-5d<sub>eg</sub>-component to stay empty above E<sub>F</sub> for coordinating H<sub>2</sub>O or HCOOH (Fig. S15) in facilitating dissociation of H<sub>2</sub>O or HCOOH.

As a substitute for Pt in the hydrogen evolution reaction (HER), Pd metal has higher reserves on Earth and exhibits suitable H-bonding energy near the peak of the volcano plot, although its performance is still not comparable with that of Pt [31]. To prove the advantage of our synthesized PdIr bimetallic for electrocatalysis, we firstly conducted HER tests of PdIr bimetallic with different Pd/Ir atomic ratios in alkaline media (Figs S16 and S17). The result shows that Ir alloying can indeed promote the HER activity of pure Pd metal. An atomic ratio of Pd/Ir at 4:1 in the PdIr bimetallic can lead to the best HER activity. Surprisingly, the optimized PdIr bimetallic/C also shows the highest onset potential among the other five catalysts, with the order of PdIr bimetallic/C > Pt/C > Ir/C > Pd/C > PdIr NP/C > Pd/C (Fig. 4a). To achieve the current density of 10 mA cm<sup>-2</sup>, the PdIr bimetallic/C

required only an overpotential of 34 mV, much smaller than that of Pt/C (72 mV), Ir/C (84 mV), PdIr NP/C (117 mV) and Pd/C (270 mV) (Fig. 4b). In electrocatalysis, the smaller Tafel slopes of the catalysts reflect the higher kinetic efficiency. The PdIr bimetallic/C shows a Tafel slope of 58.3 mV/dec, much lower than that of PdIr NP/C catalyst (107.9 mV/dec) and even lower than that of Pt/C (73.8 mV/dec), indicating accelerated HER dynamics on the PdIr bimetallic (Fig. 4c). PdIr bimetallic exhibits the highest specific activity and mass activity among those catalysts (Figs S18 and S19), in particular delivering a mass activity of 2.67 mA μg<sub>Pd</sub><sup>-1</sup> (2.06 mA μg<sub>Pd+Ir</sub><sup>-1</sup>), 2.8, 4.7 times and 33.3 times higher than those of commercial Pt/C (0.92 mA μg<sub>Pt</sub><sup>-1</sup>), PdIr NP (0.56 mA μg<sub>Pd+Ir</sub><sup>-1</sup>) and Pd/C (0.08 mA μg<sub>Pd</sub><sup>-1</sup>), presenting the best level of the HER catalysis in alkaline solution yet reported (Table S4). As is known, the HER involves two sequential steps in alkaline media: dissociation of water to get protons and recombination of protons to release H<sub>2</sub> [32]. The first step is the rate-determining step with sluggish kinetics, leading to poorer HER performance in alkaline media than in acid [32–34]. As a consequence, the origin of the superb HER

activity of PdIr bimetallic could be attributed to the enhanced water-dissociation ability of the protrusion Pd-Ir reconstructed site on the PdIr bimetallic. In accordance with the theoretical calculations, the surface Ir sites could facilitate dissociation of the OH group from the H<sub>2</sub>O to produce enough protons (Fig. S14), and then the protons are adsorbed and combined on the Pd sites, further accounting for the enhancement of the HER activity of PdIr bimetallic over Pd metallene.

The chronoamperometry technique was employed to examine the electrocatalytic stability of PdIr bimetallic. Figure 4d shows time-dependent current density retention curves of the PdIr bimetallic under static overpotential of 20 and 70 mV, respectively. After an 8 h durability test, PdIr bimetallic/C maintained 93.0% and 85.8% percentages of its original activity at 20 and 70 mV *vs* RHE, much higher than similarly calculated for commercial Pt/C (55.4% and 38.1%, Fig. S20). The Pt nanoparticle had undergone severe aggregation, whereas PdIr bimetallic was well preserved after stability testing (Fig. S21). The stability enhancement on PdIr bimetallic can be attributed to its stronger binding with carbon support than Pt nanoparticle, realized by more direct contact through the NSs structure. Meanwhile, the surface of PdIr metallene contains more atoms with low coordination, which are more stable in catalytic reaction. To further prove the stability of PdIr bimetallic over a longer time, instead of using GC electrode, we retested the HER of the PdIr bimetallic with mass loading of 0.2 mg<sub>Pd+Ir</sub> cm<sup>-2</sup> using carbon paper (CP) as electrode substrate. The chronopotentiometry of PdIr bimetallic at 10 mA cm<sup>-2</sup> (Fig. S22) showed very little decay after 75 h testing, revealing the super stability of PdIr bimetallic for HER.

As further proof of the superiority in electrocatalysis of large atomic exposure area with unique electronic structure in our synthesized PdIr bimetallic, we examined the electrocatalytic performance of PdIr bimetallic/C, Pd metallene/C, PdIr NP/C and commercial Pd/C in the formic acid oxidation reaction (FAOR). The onset potential of PdIr bimetallics all shift negatively compared with that of Pd metallene, revealing that Ir alloying on Pd metallene can accelerate the FAOR (Fig. S23). From the typical FAOR curves of optimal PdIr bimetallic/C, PdIr NP/C and commercial Pd/C (Figs 5a and S24), the PdIr bimetallic/C exhibits the lowest onset potential and highest specific activity among all the investigated catalysts, indicating its excellent intrinsic activity. Meanwhile, benefiting from the high atomic utilization, the mass activity of PdIr bimetallic/C could reach up to 2.70 A mg<sub>Pd+Ir</sub><sup>-1</sup> at a potential

of 0.5 V *vs* RHE, 3.97 and 4.82 times higher than those of PdIr NP/C (0.68 A mg<sub>Pd+Ir</sub><sup>-1</sup>) and Pd/C (0.56 A mg<sub>Pd</sub><sup>-1</sup>) (Fig. 5b). Compared with other reported Pd-based FAOR catalysts, its mass activity at peak is about 3.75 A mg<sub>Pd</sub><sup>-1</sup>, presenting the top level (Table S5).

The electrocatalytic stability of these three catalysts was further measured by chronoamperometric measurements at a constant potential of 0.5 V *vs* RHE. In Fig. 5c, the drop speeds follow with the order of PdIr bimetallic/C < PdIr NP/C < Pd/C, while the PdIr bimetallic/C is the most stable showing mass activity remaining at 0.45 A mg<sub>Pd+Ir</sub><sup>-1</sup> after 3000 s. We examined the FAOR activity again in the refreshed electrolyte after the durability test (Figs S25 and S26). We found that the mass activity of PdIr bimetallic/C remained at almost 78% at a potential of 0.5 V *vs* RHE, much higher than those of Pd metallene/C (42%), PdIr NP/C (28%) and commercial Pd/C (15%). The TEM images also show that the structure of the PdIr bimetallic is basically unchanged after the FAOR (Fig. S27).

Pathways of the FAOR on the catalysts are usually of two kinds: dehydrogenation or dehydration [35]. For the Pd-based catalysts, dehydrogenation is often the main pathway, but recent works indicate that the dehydration pathway also occurs on Pd [36]. In the latter pathway, the reaction intermediate CO adsorbs and then assembles on the surface of Pd, hindering further oxidation of the formic acid molecule, leading to fast degradation of catalytic performance under long-term FAOR conditions [37,38]. To understand the reasons for stability improvement of PdIr metallene, the CO tolerance of these catalysts was examined using the CO stripping test (Fig. 5d). It can be observed clearly that the CO oxidation peaks on PdIr NP/C show a slight negative shift compared with that on Pd/C, revealing that CO oxidation is easier on Pd when it is alloyed with Ir. Surprisingly, the CO anti-poisoning ability can be further promoted on the PdIr bimetallic, revealed by the extra negative shift of CO oxidation peaks compared with PdIr NP/C. Usually Ir metal does not possess the ability to promote electrocatalytic oxidation of formic acid while Pd metal is the active site [39]. In the case of PdIr bimetallic, with its optimal surface electronic structure, the Pd-Ir protrusions can provide extraordinarily high performance in OH dissociation and efficient docking of the leaving group (HCOO\*). The surface Ir-5d band actually provides substantial overlapping with the O-2p band, and a few overlaps with the C-2p band given from the orbital components from the HCOOH molecule (Fig. S14). This indicates that Ir sites on the top protrusion surface area can stably locate the O-part from the HCOOH for

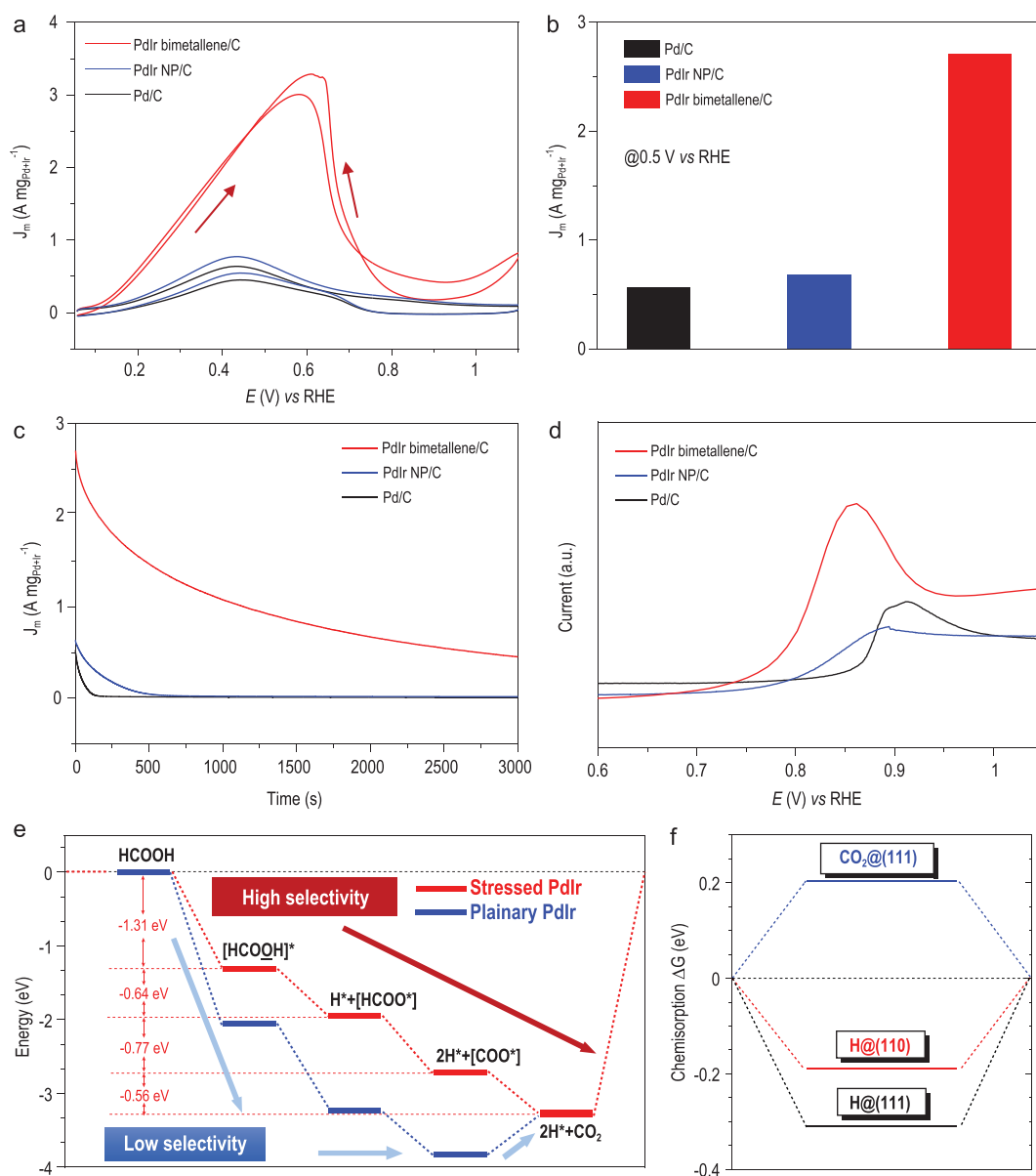


**Figure 5.** FAOR performance and enhancement mechanism of PdIr bimetallic. (a) CVs of PdIr bimetallic/C, PdIr NP/C and Pd/C for FAOR in 0.1 M HClO<sub>4</sub> containing 0.5 M HCOOH at the scan rate of 50 mV s<sup>-1</sup>. (b) Mass activities of different catalysts at the potential of 0.5 V vs RHE. (c) Chronoamperometric curves of the PdIr bimetallic/C, PdIr NP/C and Pd/C catalysts at 0.5 V vs RHE. (d) CO stripping tests of PdIr bimetallic/C, PdIr NP/C and Pd/C catalysts conducted in 0.1 M HClO<sub>4</sub> at the scan rate of 50 mV s<sup>-1</sup>. (e) Free energy pathway ( $\Delta G$ ) for FAOR under acidic conditions. (f) Chemisorption of H and CO<sub>2</sub> on the surface (111).

straightforward acidic FAOR with a large energetic gain, instead of adsorption of C site towards a catalyst poisoning reaction. Meanwhile, the Ir-O bond can further prevent local oxidation of the Pd (II) site based on promoted site-to-site electron transfer, which is significant as an electrogeneration center for enhancing HCOOH electro-oxidation.

To shed further light on the catalytic mechanism of PdIr bimetallic, the energetic pathway for FAOR was studied under acidic conditions, showing that the overall reaction heat is in a continuous

downtrend with spontaneous character of  $\Delta G < 0$ . With the reference level infinitely far away, the itinerant HCOOH molecule anchoring on the Pd<sub>8</sub>Ir<sub>2</sub> (111) surface gains an energy of -1.31 eV. This is potentially the rate-determining step as it possesses the largest energy gain overall for the FAOR process. Further strong surface adsorption reflects the OH bond dissociation with -0.64 eV decreased. Meanwhile, we found that the surface Pd-Ir protrusions enhanced further splitting of the OH that produces the step [COOH → H\* + COO\*], gaining extra

energy of  $-0.77$  eV with the existence of adsorbing  $^*H$ . In the final step when the local stably adsorbed  $2H^*$  still remained, the adsorbed  $COO^*$  turned to form  $CO_2$  gas molecules to be desorbed from the surface. In contrast to the strain-free PdIr surface, the FAOR process is more selective and energetically preferred to proceed with  $-0.56$  eV lowered (Fig. 5e). We compared the chemisorption energies of H and  $CO_2$ , respectively. It was found that H at the (111) surface reflects a negative chemisorption  $\Delta G$ , denoting a potential rather stable initial adsorption towards high H-coverage. However, the  $CO_2$  chemisorption energy shows positive chemisorption above the thermo-neutral line ( $\Delta G = 0$ ), which implies efficient desorption of  $CO_2$ . This energetic comparison can natively show suppression of further poisoning of the catalyst and secondary  $CO_2$  adsorption for oxidizing the active Pd site (Fig. 5f). Therefore, this trend guarantees an efficient FAOR and further fast rate for the HER under small overpotential. From the local structure (Fig. S27), the stable adsorbed H is bonding with the Pd site, and the HCOO group is also stably adsorbing on the Ir site at the top surface of the protrusion area. The bond-cleavage of the HO process from HCOOH occurs between the Pd and Ir sites. The two closely adsorbed  $^*H$  on the Pd sites actually contribute to the potentially efficient  $H_2$  generation. With assistance from the Ir site, the leaving group ( $HCOO^*$ ) can be stably located on the surface of  $Pd_8Ir_2$  (111).

## CONCLUSION

In summary, we report a new class of PdIr bimetalloids as an extraordinary electrocatalyst for both HER and FAOR. Super-high atom exposure and strain-induced unique electron structure on the surface contribute to the exceptional mass activity for HER in alkaline media, 33.3 times higher than that of Pd/C, representing the best reported performance of Pt-free HER catalyst yet. Furthermore, the PdIr bimetalloids shows superior activity and stability over home-made PdIr NP and commercial Pd/C towards FAOR in acid media. DFT calculations unravel formation of concave-convex featured electro-active regions by the strong surface strain effect, which directly correlate with the unique on-site  $4d^{10}$ - $t_{2g}$ -orbital Coulomb potential and propel higher orbital-electronegativity within these active regions. Such modulation has optimized the electronic environment for energetically favorable evolution of actualizing the universally excellent HER and FAOR performance. Beyond the conventional modulation of nanocatalysts, we believe the proposed strategy will innovate new inspirations for

pursuing suprathin 2D multi-metallic nanostructures with the desired surface structure and composition to extend potential applications in various fields.

## METHODS

### Synthesis of PdIr bimetalloids

In a typical preparation of PdIr bimetalloids, 10 mg  $Pd(acac)_2$ , 2.5 mg  $Ir_4(CO)_{12}$ , 30 mg  $W(CO)_6$ , 25 mg  $NH_4Br$  and 5 mL OAM were added to a 15 mL pressure bottle, and ultrasonicated to obtain a homogeneous solution. After the pressure bottle was sealed, the mixture was heated to  $150^\circ C$  and maintained at  $150^\circ C$  for 8 h in an oil bath. The cooled product was washed three times with a cyclohexane/ethanol mixture (v : v, 5 : 1) to wash off the redundant OAM. Note, the airtightness of the reaction vessel is essential to prevent volatilization of  $Ir_4(CO)_{12}$  in reaction, otherwise the atomic ratio of Pd/Ir element in end products will be much larger than that of added Pd/Ir precursor.

### Electrochemical tests

The carbon supported catalysts were dispersed in a mixture containing water, isopropanol and 5 wt% Nafion (volume ratio: 0.75 : 0.24 : 0.01) to form homogeneous ink by sonication for 60 min in an ice bath. The concentration of precious metal was controlled to be  $0.2 \text{ mg}_{\text{metal}} \text{ mL}^{-1}$  based on the ICP-AES measurement. Electrochemical tests were performed using a CHI660E electrochemical workstation (Chenhua, Shanghai) with a three-electrode system. The catalyst modified rotating disk glass carbon (GC) electrode (Pine Ins) was used as the working electrode, an Ag/AgCl (in acid) or Hg/Hg<sub>2</sub>Cl<sub>2</sub> (in base) electrode was used as the reference electrode and a Pt wire (for FAOR) or graphite rod electrode (for HER) was used as the counter electrode. All measurements were conducted at room temperature. HER tests were carried out in  $N_2$ -saturated 0.1 M KOH, and the linear sweep voltammetry was recorded at a scan rate of  $5 \text{ mV s}^{-1}$  with a rotation rate of 2000 rpm. The mass loading was controlled to be  $\sim 2 \mu\text{g}_{\text{metal}}$  on the electrode, determined by ICP-AES. The measured resistance of 0.1 M KOH was around  $43.6 \Omega$  and 95% iR drop compensation was conducted unless otherwise mentioned. Before the FAOR tests, a surface cleaning step of the catalysts was applied by CV in  $N_2$ -saturated 0.1 M HClO<sub>4</sub> at high sweep rate of  $500 \text{ mV s}^{-1}$  at a potential of 0.05–1.0 V vs RHE. Then, the FAOR tests were performed in  $N_2$ -saturated 0.1 M HClO<sub>4</sub> + 0.5 M HCOOH. Cyclic voltammetry was applied to evaluate the performance of catalysts at a rate of

50 mV s<sup>-1</sup>. The chronoamperometry technique was used to investigate the stability of catalysts. The ECSA was determined by integrating the charge of underpotentially deposited H and stripping of CO. All electrochemical data were tested for at least three times. For the CO stripping tests, the experiments were carried out in 0.1 M HClO<sub>4</sub>. Before the test, the solution was purged with Ar for 20 min to remove the O<sub>2</sub> in the solution, and then bubbled with CO gas (99.9%) for 10 min at 0.1 V vs RHE. The residual CO in the solution was excluded by Ar for another 20 min.

## SUPPLEMENTARY DATA

Supplementary data are available at [NSR](#) online.

## FUNDING

This work was supported by the National Science Fund for Distinguished Young Scholars (52025133), the Tencent Foundation through the XPLOER PRIZE, the Beijing Natural Science Foundation (JQ18005) and the Fund of the State Key Laboratory of Solidification Processing in NWPU (SKLSP202004). Electron microscopy (EM) work used resources of the Center for Functional Nanomaterials, which is a US DOE Office of Science Facility, at Brookhaven National Laboratory under Contract No. DE-SC0012704.

## AUTHOR CONTRIBUTIONS

S.G. proposed and supervised the project. S.G. and F.L. conceived and designed the experiments. F.L. and J.F. carried out the synthesis and most of the structural characterizations. F.L., W.Z., K.W. and J.Z. performed the electrochemical tests. B.H. carried out DFT calculations. N.L., Y.D. and D.S. performed the HAADF-STEM characterizations and EELS experiments. Z.P. and W.Y. participated in EXAFS experiment and data processing. S.G., B.H. and F.L. co-wrote the manuscript. All the authors discussed the results and participated in analyzing the experimental results.

**Conflict of interest statement.** None declared.

## REFERENCES

- Roger I, Shipman MA and Symes MD. Earth-abundant catalysts for electrochemical and photoelectrochemical water splitting. *Nat Rev Chem* 2017; **1**: 1–13.
- Cheng W, Zhao X and Su H *et al.* Lattice-strained metal-organic-framework arrays for bifunctional oxygen electrocatalysis. *Nat Energy* 2019; **4**: 115–22.
- Suen NT, SF H and Quan Q *et al.* Electrocatalysis for the oxygen evolution reaction: recent development and future perspectives. *Chem Soc Rev* 2017; **46**: 337–65.
- Seh ZW, Kibsgaard J and Dickens CF *et al.* Combining theory and experiment in electrocatalysis: insights into materials design. *Science* 2017; **355**: eaad4998.
- Duchesne PN, Li ZY and Deming CP *et al.* Golden single-atomic-site platinum electrocatalysts. *Nat Mater* 2018; **17**: 1033–9.
- Li M, Zhao Z and Cheng T *et al.* Ultrafine jagged platinum nanowires enable ultrahigh mass activity for the oxygen reduction reaction. *Science* 2016; **354**: 1414–9.
- Chen C, Kang Y and Huo Z *et al.* Highly crystalline multimetallic nanoframes with three-dimensional electrocatalytic surfaces. *Science* 2014; **343**: 1339–43.
- Feng JR, Lv F and Zhang WY *et al.* Iridium-based multimetallic porous hollow nanocrystals for efficient overall-water-splitting. *Adv Mater* 2017; **29**: 1703798.
- Huang L, Zhang X and Wang Q *et al.* Shape-control of Pt–Ru nanocrystals: tuning surface structure for enhanced electrocatalytic methanol oxidation. *J Am Chem Soc* 2018; **140**: 1142–7.
- Huang XQ, Zhao Z and Cao L *et al.* High-performance transition metal-doped Pt<sub>3</sub>Ni octahedra for oxygen reduction reaction. *Science* 2015; **348**: 1230–4.
- Escudero-Escribano M, Malacrida P and Hansen MH *et al.* Tuning the activity of Pt alloy electrocatalysts by means of the lanthanide contraction. *Science* 2016; **352**: 73–6.
- Li Q, Wu L and Wu G *et al.* New approach to fully ordered fct-FePt nanoparticles for much enhanced electrocatalysis in acid. *Nano Lett* 2015; **15**: 2468–73.
- Jin H, Guo C and Liu X *et al.* Emerging two-dimensional nanomaterials for electrocatalysis. *Chem Rev* 2018; **118**: 6337–408.
- Sial M, Din MAU and Wang X. Multimetallic nanosheets: synthesis and applications in fuel cells. *Chem Soc Rev* 2018; **47**: 6175–200.
- Chen Y, Fan Z and Zhang Z *et al.* Two-dimensional metal nanomaterials: synthesis, properties, and applications. *Chem Rev* 2018; **118**: 6409–55.
- Luo M, Yang Y and Sun Y *et al.* Ultrathin two-dimensional metallic nanocrystals for renewable energy electrocatalysis. *Mater Today* 2019; **23**: 45–56.
- Chia X and Pumera M. Characteristics and performance of two-dimensional materials for electrocatalysis. *Nat Catal* 2018; **1**: 909–21.
- Stamenkovic VR, Fowler B and Mun BS *et al.* Improved oxygen reduction activity on Pt<sub>3</sub>Ni (111) via increased surface site availability. *Science* 2007; **315**: 493–7.
- Stoerzinger KA, Rao RR and Wang XR *et al.* The role of Ru redox in pH-dependent oxygen evolution on rutile ruthenium dioxide surfaces. *Chem* 2017; **2**: 668–75.
- Zhang W, Wang L and Liu H *et al.* Integration of quantum confinement and alloy effect to modulate electronic properties of RhW nanocrystals for improved catalytic performance toward CO<sub>2</sub> hydrogenation. *Nano Lett* 2017; **17**: 788–93.
- Liu Y, Xiao C and Huang P *et al.* Regulating the charge and spin ordering of two-dimensional ultrathin solids for electrocatalytic water splitting. *Chem* 2018; **4**: 1263–83.
- Deng S, Sumant AV and Berry V. Strain engineering in two-dimensional nanomaterials beyond graphene. *Nano Today* 2018; **22**: 14–35.
- Wang L, Zeng Z and Gao W *et al.* Tunable intrinsic strain in two-dimensional transition metal electrocatalysts. *Science* 2019; **363**: 870–4.

24. Luo M, Zhao Z and Zhang Y *et al.* PdMo bimetallic for oxygen reduction catalysis. *Nature* 2019; **574**: 81–5.
25. Duan H, Yan N and Yu R *et al.* Ultrathin rhodium nanosheets. *Nat Commun* 2014; **5**: 3093.
26. Huang X, Li S and Huang Y *et al.* Synthesis of hexagonal close-packed gold nanostructures. *Nat Commun* 2011; **2**: 292.
27. Park J, Sa YJ and Baik H *et al.* Iridium-based multimetallic nanoframe@nanoframe structure: an efficient and robust electrocatalyst toward oxygen evolution reaction. *ACS Nano* 2017; **11**: 5500–9.
28. Hong JW, Kim Y and Wi DH *et al.* Ultrathin free-standing ternary-alloy nanosheets. *Angew Chem In Ed* 2016; **55**: 2753–8.
29. Yun Q, Lu Q and Li C *et al.* Synthesis of PdM (M = Zn, Cd, ZnCd) nanosheets with an unconventional face-centered tetragonal phase as highly efficient electrocatalysts for ethanol oxidation. *ACS Nano* 2019; **13**: 14329–36.
30. Gao F, Zhang Y and Ren F *et al.* Universal surfactant-free strategy for self-standing 3D tremella-like PdM (M = Ag, Pb, and Au) nanosheets for superior alcohols electrocatalysis. *Adv Funct Mater* 2020; **30**: 2000255.
31. Zhang L, Chang Q and Chen H *et al.* Recent advances in palladium-based electrocatalysts for fuel cell reactions and hydrogen evolution reaction. *Nano Energy* 2016; **29**: 198–219.
32. Liao H, Wei C and Wang J *et al.* A multisite strategy for enhancing the hydrogen evolution reaction on a nano-Pd surface in alkaline media. *Adv Energy Mater* 2017; **7**: 1701129.
33. Wang P, Zhang X and Zhang J *et al.* Precise tuning in platinum-nickel/nickel sulfide interface nanowires for synergistic hydrogen evolution catalysis. *Nat Commun* 2017; **8**: 14580.
34. Zheng Y, Jiao Y and Vasileff A *et al.* The hydrogen evolution reaction in alkaline solution: from theory, single crystal models, to practical electrocatalysts. *Angew Chem In Ed* 2018; **57**: 7568–79.
35. Zhang J, Wang T and Liu P *et al.* Efficient hydrogen production on MoNi<sub>4</sub> electrocatalysts with fast water dissociation kinetics. *Nat Commun* 2017; **8**: 15437.
36. Zhang J, Chen M and Li H *et al.* Stable palladium hydride as a superior anode electrocatalyst for direct formic acid fuel cells. *Nano Energy* 2018; **44**: 127–34.
37. Wang JY, Zhang HX and Jiang K *et al.* From HCOOH to CO at Pd electrodes: a surface-enhanced infrared spectroscopy study. *J Am Chem Soc* 2011; **133**: 14876–9.
38. Xi Z, Li J and Su D *et al.* Stabilizing CuPd nanoparticles via CuPd coupling to WO<sub>2.72</sub> nanorods in electrochemical oxidation of formic acid. *J Am Chem Soc* 2017; **139**: 15191–6.
39. Wang X, Tang Y and Gao Y *et al.* Carbon-supported Pd–Ir catalyst as anodic catalyst in direct formic acid fuel cell. *J Power Sources* 2008; **175**: 784–8.